

# Revisiting Jet Clustering Algorithms for New Higgs Boson Searches in Hadronic Final States

A. Chakraborty<sup>\*1</sup>, S. Dasmahapatra<sup>†2</sup>, H.A. Day-Hall<sup>‡3,4</sup>, B. Ford<sup>§3</sup>,  
S. Jain<sup>¶3</sup>, S. Moretti<sup>||3,4</sup>, E. Olaiya<sup>\*\*4</sup>, C.H. Shepherd-Themistocleous<sup>††4</sup>

<sup>1</sup>*Centre for High Energy Physics, Indian Institute of Science,  
Bengaluru, Karnataka 560012, India*

<sup>2</sup>*School of Electronics and Computer Science, University of Southampton,  
Southampton, SO17 1BJ, United Kingdom*

<sup>3</sup>*School of Physics and Astronomy, University of Southampton,  
Southampton, SO17 1BJ, United Kingdom*

<sup>4</sup>*Particle Physics Department, Rutherford Appleton Laboratory,  
Chilton, Didcot, Oxon OX11 0QX, United Kingdom*

## Abstract

We assess the performance of different jet-clustering algorithms, in the presence of different resolution parameters and reconstruction procedures, in resolving fully hadronic final states emerging from the chain decay of the discovered Higgs boson into pairs of new identical Higgs states, the latter in turn decaying into bottom-antibottom quark pairs. We show that, at the Large Hadron Collider (LHC), both the efficiency of selecting the multi-jet final state and the ability to reconstruct from it the masses of the Higgs bosons (potentially) present in an event sample depend strongly on the choice of acceptance cuts, jet-clustering algorithm as well as its settings. Hence, we indicate the optimal choice of the latter for the purpose of establishing such a benchmark Beyond the SM (BSM) signal.

---

\*E-mail: achakraborty@iisc.ac.in

†E-mail: sd@ecs.soton.ac.uk

‡E-mail: hadh1g17@soton.ac.uk

§E-mail: b.ford@soton.ac.uk

¶E-mail: s.jain@soton.ac.uk

||E-mail: stefano@phys.soton.ac.uk

\*\*E-mail: emmanuel.olaiya@stfc.ac.uk

††E-mail: claire.shepherd@stfc.ac.uk

# 1 Introduction

Several BSM scenarios with an enlarged Higgs sector allow for the existence of additional neutral Higgs boson states, CP-even or CP-odd, which are lighter than the SM-like Higgs boson discovered at the LHC in 2012, which has a mass of approximately 125 GeV [1]. These new physics frameworks are ubiquitous in non-minimal models of Supersymmetry (SUSY) [2], in particular, but not only, in the Next-to-Minimal Supersymmetric Standard Model (NMSSM) [3]. If one departs from SUSY and remains with low-energy models, a BSM framework including these states in its particle spectrum is the Two-Higgs Doublet Model (2HDM) [4–6]. Herein, two complex Higgs doublet fields carrying eight degrees of freedom realise Electro-Weak Symmetry Breaking (EWSB) through the Higgs mechanism. Once three of these degrees of freedom are used to give mass to the  $Z$  and  $W^\pm$  bosons of the SM, five physical Higgs states survive, labelled as  $h$ ,  $H$  (which are CP-even with, conventionally,  $m_h < m_H$ ),  $A$  (which is CP-odd) and a pair of charged states with mixed CP properties,  $H^\pm$ . Of the two CP-even states, the heavier one,  $H$ , can be identified as the SM-like one and either or both the  $h$  and  $A$  states can, in comparison, be lighter over a significant region of the 2HDM parameter space (for which full mapping is completed by two additional parameters: the ratio of the Vacuum Expectation Values (VEVs) of the two doublet fields, denoted by  $\tan\beta$ , and the mixing angle between the two CP-even states, labelled as  $\alpha$ ). In fact, it is possible to find 2HDM configurations where one can have  $m_h < m_H/2$  or  $m_A < m_H/2$  (when not both), so that  $H \rightarrow hh$  and/or  $H \rightarrow AA$  decays can take place.

As a consequence of these possible decays, a process to which the LHC may have sensitivity (depending on the 2HDM’s own existence and its parameter configuration) is  $gg \rightarrow H \rightarrow hh$ , which would be resonant whenever  $m_h < m_H/2$ , thus enhanced through a Breit-Wigner (BW) dependence of the  $H$  propagator. For a  $h$  state with a mass of order 60 GeV or less, the dominant decay mode in a 2HDM is bottom-antibottom quark pairs [7, 8], i.e.,  $h \rightarrow b\bar{b}$ , so that the final state emerging from the hard scattering above is made up, at the partonic level, of four (anti)quarks<sup>1</sup>, see Fig. 1. However, due to the confinement properties of Quantum Chromo-Dynamics (QCD), the partonic stage is not accessible by experiment, only the hadronic “jets” emerging at the end of the parton shower and hadronisation phase are seen.

In order to model the (anti)quark to jet (i.e., parton to hadron) transition, “jet clustering algorithms” are currently used. The purpose of a jet clustering algorithm is to reduce the complexity of the final state, by simplifying a multi-hadronic one (in fact,

---

<sup>1</sup>Notice that the same argument can be made for the case of  $gg \rightarrow h \rightarrow AA \rightarrow b\bar{b}b\bar{b}$  when  $m_A < m_H/2$ .

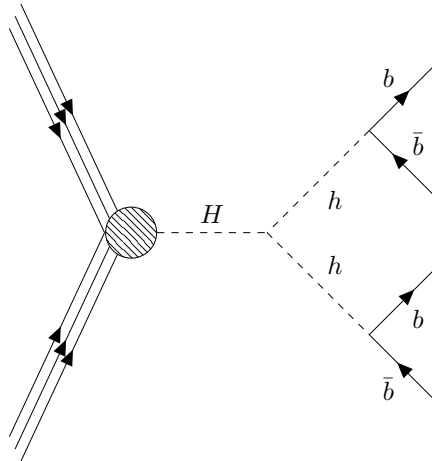


Figure 1: The 2HDM process of interest, where the SM-like Higgs state ( $m_H = 125$  GeV) produced from gluon-gluon fusion decays into a pair of lighter scalar Higgs states,  $hh$ , each in turn decaying into  $b\bar{b}$  pairs giving a four  $b$  final state.

possibly also containing photons, electrons and/or muons) into one containing objects (indeed, jets) whose properties one can calculate reliably using QCD. In essence, a typical jet clustering algorithm maps the four-momenta of the final state particles seen in the detector into a smaller number of jet four-momenta, by invoking three elements: the order in which the original momenta are combined (normally in pairs), a resolution parameter (and its numerical value) which decrees whether a pair of pseudojets (individual final state hadrons or groups of two or more hadrons which have already been combined) ought to be combined or otherwise (this then also controls the extension of the final jets over the phase space) and a recombination procedure (i.e., how the two four-momenta should combine in a cluster). The iterations of this sequence are interrupted when no more clusters can be made, so that the surviving ones are called jets and their number gives the jet multiplicity of the event.

Needless to say, there are a variety of jet clustering algorithms available and we will dwell at length on these in a forthcoming section. The purpose of this paper is to identify which jet clustering algorithm is best suited to extracting the aforementioned Higgs production and decay process in an LHC experiment. The reason for doing so is twofold. On the one hand, current recommendations (within an experiment or indeed from a theoretical perspective) on the choice of the jet clustering algorithm to use and what settings (i.e., clustering order, resolution and/or recombination scheme) to adopt

for the latter have not been made with the specific physics that we have studied here in mind, as they have emerged from the need of addressing best performance in the case of a wider variety of hadronic final states. On the other hand, the four  $b$  final state that we are invoking here is an ubiquitous signal of BSM Higgs boson pairs which are lighter than the SM one so that they can be produced from it<sup>2</sup>, crucially giving access (through the extraction of the  $h$  state properties) to key features of the underlying BSM scenario, e.g., in the form of the shape of the Higgs potential, hence, of the vacuum stability and perturbative phases of it. We are therefore motivated to pursue a dedicated treatment of the discussed final state.

Another key feature of the hadronic final state initiated by  $b$ -quarks that we intend to study is that the emerging jets can be “tagged” as such, unlike the case of lighter (anti)quarks and gluons, which are largely indistinguishable from each other. We employ a simplified method of tagging using Monte Carlo truth information, along with a probabilistic implementation of inefficiencies. For a full discussion on  $b$ -tagging at detectors, we refer the reader to [9].

Finally, in recent years, there have been advancements to established jet reconstruction techniques. In particular, we note the modification to traditional sequential combinations algorithms employing a variable inter-jet distance measure [10] (so-called ‘variable- $R$ ’ algorithms). We will therefore also investigate whether such variable- $R$  jets can improve the ability to observe particular 2HDM-II four  $b$ -jet final state topologies.

The layout of the paper is as follows. In the next section, we describe how we performed jet reconstruction and  $b$ -tagging as well as discuss the tools used for our simulations. In the following one, we present our results for both signal and background. Then, we conclude.

## 2 Methodology

### 2.1 Jet Clustering Algorithms

In order to extract proper physics from hadronic sprays found in particle detectors, algorithms are deployed to characterise the detected radiation into distinguishable objects, the aforementioned jets. There is in fact a rich history associated with the development and evolution of algorithms for jet definition, beginning in 1977 with Serman and Weinberg [11], initially deployed in the context of  $e^+e^- \rightarrow$  hadron scatterings.

---

<sup>2</sup>Here, ubiquitous refers to the fact that this signal is very typical of a variety of BSM scenarios (as explained in the Introduction), so that we effectively use the 2HDM for illustration purposes. Our results can therefore be applied to the case of other new physics models.

Jets were initially defined via two input parameters, the energy and angle of radiation, given by  $\epsilon$  and  $\delta$ , respectively. If a fraction  $1 - \epsilon$  of the total energy of the event is focused within two cones of half angle  $\delta$ , the radiation is said to be resolved into a distinguishable jet. This was the first example of a ‘cone algorithm’, which classifies jets by the geometric distribution of energy in an event and was extensively used till the mid nineties. Thanks to computational developments, the type of algorithms utilised since then have become more complex, as they are sequential recombination algorithms, called ‘jet clustering algorithms’ [12]. Rather than categorising the entire event at once, each particle in the event is considered and all are iteratively combined together based on some inter-particle distance measure, until all particles are gathered into stable jets.

Into the present day, all types of jet clustering algorithms deployed at the LHC take a similar form, descending from the generalised  $k_T$  algorithm used initially in  $e^+e^-$  colliders [12]. This uses an inter-particle distance measure which can be written in the form

$$d_{ij} = \min(p_{Ti}^n, p_{Tj}^n) \Delta R_{ij}^2, \quad (1)$$

where  $\Delta R_{ij}^2 = (y_i - y_j)^2 - (\phi_i - \phi_j)^2$  is the angular separation between particle  $i$  and  $j$ , with  $y$  and  $\phi$  being the rapidity and azimuth of the associated final state hadron. They also make use of the ‘beam distance’, which is the separation of object  $i$  and the beam  $B$

$$d_{Bi} = p_{Ti}^n R^2. \quad (2)$$

Note that we use the same notation as in [10], where  $R^2$  is included in the definition of  $d_{Bi}$ . (An alternative convention is to embed  $R^2$  into the definition of  $d_{ij}$  such that  $d_{ij} = \min(p_{Ti}^n, p_{Tj}^n) \frac{\Delta R_{ij}^2}{R^2}$ , leaving  $d_{Bi} = p_{Ti}^n$ , like in [13].) For a set of particles, all possible  $d_{ij}$ ’s and  $d_{Bi}$ ’s are calculated and the minimum is taken. If the minimum is a  $d_{ij}$ , objects  $i$  and  $j$  are combined and the process is repeated. If, instead, a  $d_{Bi}$  is the minimum, then  $i$  is declared a jet and removed from the sample. This procedure is then repeated until all objects are classified into jets.

In  $d_{Bi}$ ,  $R$  is a fixed input variable which dictates the size of the jet and acts as the cut-off for any particle pairing. If we consider some pair of particles  $i$  and  $j$ , with  $i$  having lower  $p_T$  (and hence being selected in  $d_{ij}$ ), we can write (for  $n \geq 0$ )

$$d_{ij} = \Delta R_{ij}^2 p_{Ti}^n = \frac{\Delta R_{ij}^2}{R^2} d_{Bi}. \quad (3)$$

Since we require the ratio  $\frac{\Delta R_{ij}^2}{R^2} < 1$  to avoid declaring  $i$  a jet over merging  $i$  with  $j$ , we can see that  $R$  acts as an effective cut off for the maximum separation of two pseudojets to be combined and, hence, it is proportional to the final jet size. From this general

formulation, the main two jet clustering algorithms currently in use at the LHC are the Cambridge-Aachen (CA) [14, 15] one and the anti- $k_T$  [16] one, which use the above expressions with  $n = 0$  and  $-2$ , respectively [17].

## 2.2 Jet Clustering with Variable- $R$

There has in fact been a more recent development to these techniques. One notices that the above algorithms require as input a fixed parameter,  $R$ , which in the case of the anti- $k_T$  algorithm effectively acts as the jet radius<sup>3</sup>. Recall this acts as a cut off for combining hadrons and can therefore be interpreted as implementing a size limit on the jets depending on the particle separation.

The angular spread of the final jet constituents has a dependence on the initial partons  $p_T$ . For higher  $p_T$  objects the decay products will be more tightly packed into a more collimated cone whereas for low  $p_T$  objects one would expect the resulting jet constituents to be spread over some wider angle. One can therefore imagine the need for carefully selecting the  $R$  value used for clustering depending on the  $p_T$  of the final state jets, but what about in a multi-jet scenario where the final state partons have a wide range of  $p_T$ 's?

The aforementioned variable- $R$  jet clustering algorithm [10] alters the above scheme so as to adapt to events with jets of varying cone size. A modification to the distance measure  $d_{ij}$  is made, by replacing the fixed input parameter  $R$  with a  $p_T$  dependent  $R_{\text{eff}}(p_T) = \frac{\rho}{p_T}$ , where  $\rho$  is a chosen dimensionful constant (taken to be  $\mathcal{O}(\text{jet } p_T)$ ). With this replacement, the beam distance measure becomes

$$d_{Bi} = p_{Ti}^n R_{\text{eff}}(p_{Ti})^2. \quad (4)$$

When the distance measures are calculated,  $d_{Bi}$  will therefore be suppressed for objects with larger  $p_T$  and hence these objects become more likely to be classified as jets. For low  $p_T$  objects,  $d_{Bi}$  is enhanced and so these are more likely to be combined with a near neighbour, thus increasing the spread of constituents in the eventual jet.

We hypothesise therefore that, in multijet signal events where one might expect signal  $b$ -jets with a wide spread of different  $p_T$ 's, a variable- $R$  reconstruction procedure could improve upon the performance of traditional fixed  $R$  routines. In particular, using

---

<sup>3</sup>It is an important distinction to notice that  $R$  only looks like a cone parameter for the anti- $k_T$  algorithm ( $n = -2$ ). In this case, the 'min' in Eq. (1) picks out the larger  $p_T$  pseudojet. If we take  $i$  as the higher  $p_T$  object, then, if  $j$  is further from  $i$  than  $R$ ,  $i$  and  $j$  will not be combined. In other words, if  $i$  is close to the eventual jet axis, low momenta  $j$ 's will not be included, so that in the end  $R$  effectively ends up as the jet radius. While this point is important, we also note that we mostly use the anti- $k_T$  algorithm in this study and so referring to  $R$  as an effective cone size is largely justified.

a variable- $R$  alleviates the balancing act of finding a single fixed cone size that suitably engulfs all of the radiation inside a jet, without sweeping up too much outside ‘junk’.

As a brief visualisation, we can map the constituents of  $b$ -tagged jets in the same event, which have been clustered using both a variable- $R$  and fixed  $R = 0.4$  scheme, as seen in Fig. 2. We notice that for the leading and sub-leading  $b$ -jets, the jet content is roughly the same. For the lower  $p_T$  jets however, the variable- $R$  jets gather a wider cone of constituents. The loss of constituents will harm our ability to accurately reconstruct Higgs masses when analysing  $b$ -jets. In Fig. 3 we see a case where using a larger fixed cone ( $R = 0.8$ ), to try and gather all of the constituents, only resolves three  $b$ -jets. Variable- $R$  however ‘finds’ all four  $b$ -jets expected from the signal. We can see that the fixed cone sweeps radiation from a nearby jet into the leading  $b$ -jet, whereas variable- $R$  is able to resolve both due to the larger  $p_T$  (and hence smaller  $R_{\text{eff}}$ ) of the leading  $b$ -jet, while also having a large enough cone to suitably reconstruct the lower  $p_T$  jets.

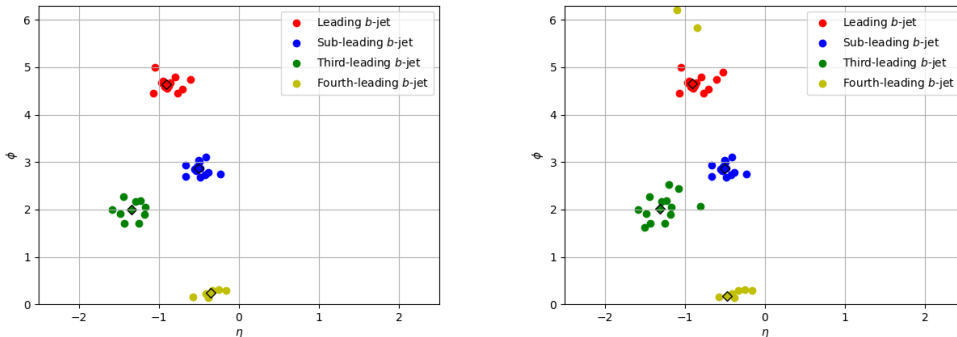


Figure 2: The same Monte Carlo (MC) event in  $(\eta, \phi)$  space. Tracks have been clustered with (left) a fixed  $R = 0.4$  and (right) variable- $R$  algorithm. The coloured points are the constituents of the corresponding  $b$ -tagged jet in the legend and black outlined diamonds are at the overall  $(\eta, \phi)$  coordinates of the formed  $b$ -jet. The anti- $k_T$  algorithm is used in both cases.

### 2.3 Implementation of $b$ -Tagging

In this paper we implement a MC informed  $b$ -tagger. For events clustered using a fixed- $R$  cone size, jets within angular distance  $R$  from each parton level  $b$ -(anti)quark are searched for and tagged as appropriate. For scenarios where multiple jets are found, the

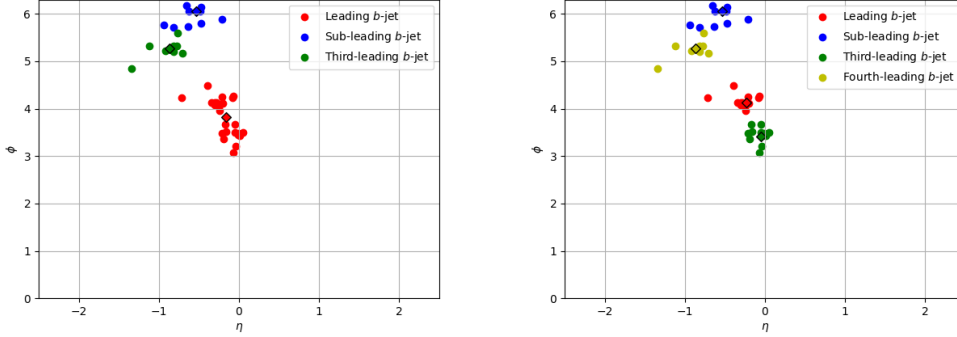


Figure 3: Same plot as in Fig. 2, however, here, the given event is clustered into three  $b$ -jets when a fixed  $R = 0.8$  is used (left) and four  $b$ -jets when we use a variable- $R$  approach (right).

closest is taken as the assignee for the  $b$ -tag. When the variable- $R$  approach is used, the size of the tagging cone is taken as the effective size of the jet  $R_{\text{eff}}$  defined above.

In addition, when we consider the signal and background rates, we account for the finite efficiency of identifying a  $b$ -jet as well as the non-zero probability that  $c$ -jets and light-flavour plus gluon jets are mistagged as  $b$ -jets. We do so by firstly running jets through the MC  $b$ -tagger described above. However, in order to mimic finite efficiency effects, jets coming from  $b$ -(anti)quarks are then  $b$ -tagged with a 75% success rate. As for jets emerging from  $c$ -(anti)quarks, we assign to these a 10%  $b$ -mistag rate. Finally, the remaining jets (lighter (anti)quark and gluon ones) have a 1%  $b$ -mistag rate applied.

The efficiencies described above are in line with the current rates at CMS, using the CMS  $b$ -tagger DeepCSV [18], which quotes values of the  $b$ -tag efficiency rate,  $c$ -jet  $b$ -mistag rate and light jet mistag rate of 68%, 12% and 1.1%, respectively. Furthermore, there is the CMS DeepJet tagger [19] which outperforms the DeepCSV tagger and shows that  $b$ -tagging efficiencies higher than 68% are reasonable.

We begin our analysis with a strict  $p_T$  cut on  $b$ -jets of at least 30 GeV. However, due to the rate at which signal is lost with these cuts, we try a lighter  $p_T$  cutflow informed by the  $bb\mu^+\mu^-$  exotic Higgs analysis by CMS [20]. Here, the  $p_T$  of the leading  $b$ -jet is required to be  $> 20$  GeV and the other  $p_T > 15$  GeV. This reduced cutflow would require the implementation of a trigger with  $p_T$  thresholds of 15, 10, 10 and 10 GeV for the four ( $p_T$  ordered)  $b$ -jets. These  $p_T$  thresholds are sufficiently below our jet  $p_T$  requirement to enable 100% efficiency in the trigger.

## 2.4 Simulation Details

We consider two sample benchmark points, namely,  $m_h = 40$  GeV and 60 GeV, while fixing  $m_H = 125$  GeV, within a 2HDM Type-II (2HDM-II henceforth), which have been tested against theoretical and experimental constraints by using 2HDMC [21], HiggsBounds [22], HiggsSignals [23] as well as checking flavour constraints with SuperISO [24]. We generate samples of  $\mathcal{O}(10^5)$  events, with  $\sqrt{s} = 13$  TeV. The production and decay rates for the process  $pp \rightarrow H \rightarrow hh \rightarrow b\bar{b}b\bar{b}$  are presented in Tab. 1, alongside the 2HDM-II input parameters. (Notice that the  $H$  and  $h$  decay widths are of order MeV, hence much smaller than the detector resolutions in two- and four-jet invariant masses, respectively, so that the Higgs states can essentially be treated as on-shell.) In the calculation of the overall cross section, the renormalisation and factorisation scales were both set to be  $H_T/2$ , where  $H_T$  is the sum of the transverse energy of each parton. The Parton Distribution Function (PDF) set used was NNPDF23\_lo\_as\_0130\_qed [25]. Finally, in order to carry out a realistic MC simulation, the toolbox described in Fig. 4 was used to generate and analyse events [26–29]<sup>4</sup>.

$m_h$ (GeV)	$m_A$ (GeV)	$m_{H^\pm}$ (GeV)	BR( $H \rightarrow hh$ )	BR( $h \rightarrow b\bar{b}$ )	$\sigma$ (pb)
40	600	600	$3.231 \times 10^{-2}$	$9.066 \times 10^{-1}$	$3.542 \times 10^{-1}$
60	620	400	$6.764 \times 10^{-1}$	$8.610 \times 10^{-1}$	6.688

Table 1: The 2HDM-II parameters and cross sections of the process in Fig. 1 used here. Note that in both cases we fix  $\lambda_6 = \lambda_7 = 0$ ,  $m_{12}^2 = 4000$  GeV<sup>2</sup>,  $\tan\beta = 1.6$ ,  $\sin(\beta - \alpha) = 0.1$  and  $m_H = 125$  GeV (in line with the SM-like Higgs measurements).

Before introducing the sequences of cuts that we have adopted here, some discussions are in order on their possible choice, as intimated in the previous section. In existing four  $b$ -jet analyses by the ATLAS and CMS collaborations, seeking to extract chain decays of Higgs bosons like the ones considered here from the background, rather restrictive cuts have been used for the ensuing fully hadronic signature. Taking CMS as an example, upon enforcing the same  $p_T$  cuts on  $b$ -jets as in Ref. [30], which are as shown in Fig. 5, we noticed that the signal selection efficiency was too low (in various respects, as described later) to enable one to create a MC sample suitable for experimental analysis assuming

---

<sup>4</sup>Note that we use the Leading Order (LO) normalisation for the signal cross sections here, for consistency with the fact that most of the background ones in our forthcoming analysis are only implemented at LO. While this affects our final results on event rates and significances, we re-instate here that the main purpose of our paper is to assess the jet clustering performance, rather than the exact values of signal and backgrounds rates.

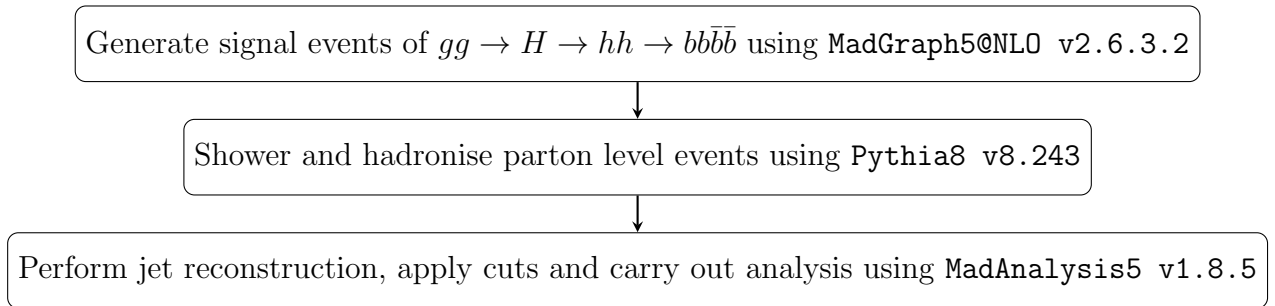


Figure 4: Description of the procedure used to generate and analyse MC events.

Run 2 and 3 luminosities. We explored the possibility of using lower  $p_T$  cuts on the jets and finally used  $p_T$  cuts used by the CMS experiment in the analysis of  $b\bar{b}\mu^+\mu^-$  final states (also emerging from Higgs cascade decays) of Ref. [20]. We thus replaced the starred (\*) cut  $p_T > 30$  GeV on each reconstructed  $b$ -jet in Fig. 5 as described in Sec. 2.3 with a cut of  $p_T > 20$  GeV for the leading  $b$ -jet with all others required to have  $p_T > 15$  GeV. We will discuss the pros and cons of each of the cutflows in the forthcoming section.

## 3 Results

In this section we present the results for our signal at both the parton and detector level. In the latter case, we also discuss the dominant backgrounds, due to QCD  $4b$  production,  $gg, q\bar{q} \rightarrow Zb\bar{b}$  and  $gg, q\bar{q} \rightarrow t\bar{t}$ <sup>5</sup>.

### 3.1 Parton Level Analysis

At the Matrix Element (ME) level, all the events have four  $b$ -quarks originating from the decay of the two light Higgs bosons ( $h$ ). The mass difference between the heavy and light Higgs states leads to boosted  $b$ -quarks, therefore, we plot the  $R$  separation between the  $b$ -quarks coming from the same light Higgs state (see upper panel of Fig. 6). The two distributions corresponding to  $m_h = 40$  and 60 GeV are markedly different. This can be understood as follows. In general, the angular separation between the decay products  $a$

<sup>5</sup>In fact, we have checked that the additional noise due to  $t\bar{t}b\bar{b}$  events as well as hadronic final states emerging from  $W^+W^-$ ,  $W^\pm Z$  and  $ZZ$  production and decay are negligible, once mass reconstruction around  $m_h$  and  $m_H$  is enforced.

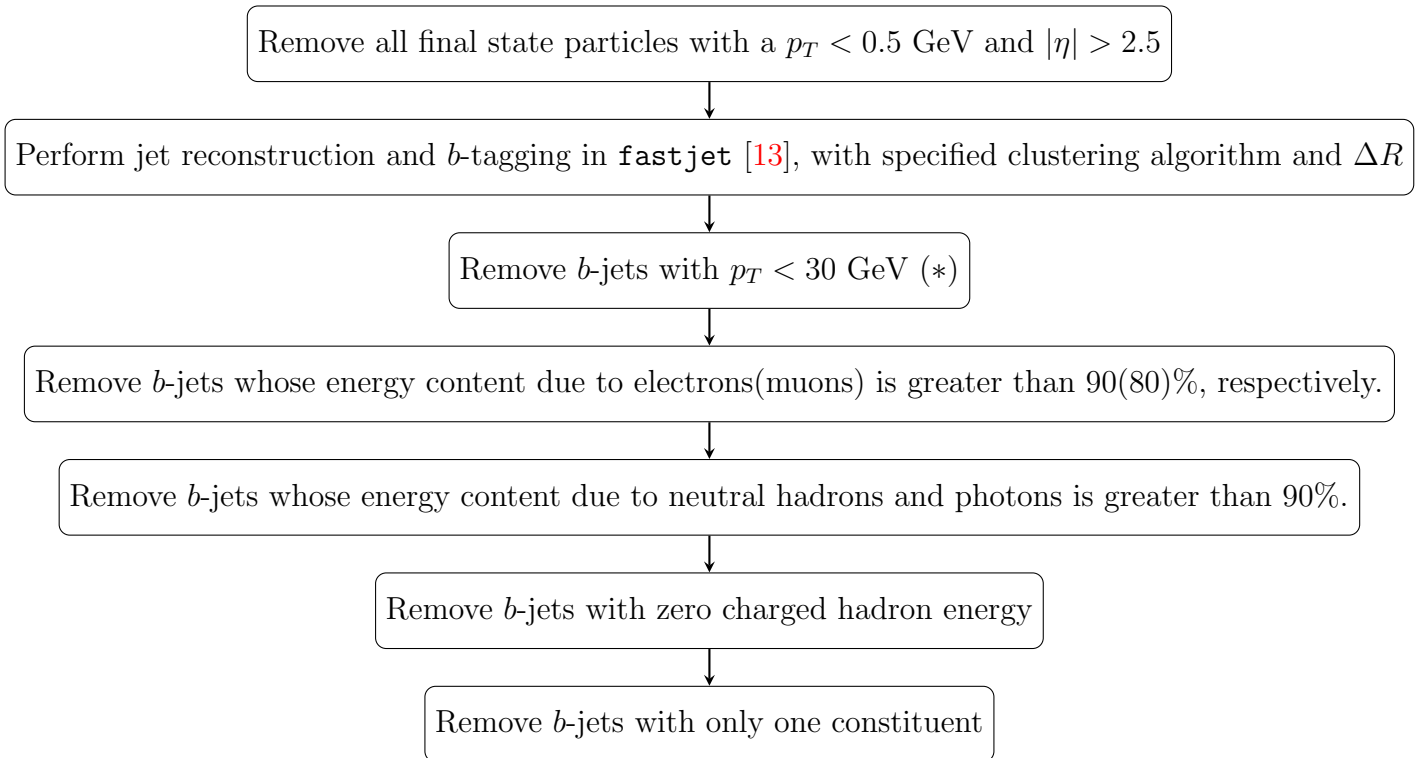


Figure 5: Description of our initial procedure for jet clustering,  $b$ -tagging and selection of jets. Notice that the starred cut (\*) will eventually be modified in our optimised  $b$ -jet selection. Also note that our analysis is performed at particle level rather than detector, so truth level MC information is used for cuts on jet constituents.

and  $b$  in the resonant process  $X \rightarrow ab$  can be approximated as  $\Delta R(a, b) \sim \frac{2m_X}{p_T^X}$ . Hence, we plot in the lower left panel of Fig. 6 the transverse momentum of each of the  $h$  bosons. For  $m_h = 60$  GeV, the light Higgs boson has less  $p_T$  than for lower values (owing to the smaller  $m_H - m_h$  mass difference), therefore, the  $b$ -quarks are more widely separated in this case, compared to  $m_h = 40$  GeV. In the light of this, we can already conclude that there is a strong correlation between the lightest Higgs boson mass and the cone size of the jet clustering algorithm that ought to be used. In particular, we can say that, in order to maximise the number of jets<sup>6</sup> for different choices of the light Higgs boson mass, we need to vary the jet radius parameter. That is, a fixed jet radius parameter may not be suitable here for all  $m_h$  choices. In the lower right panel of Fig. 6, we finally

<sup>6</sup>This is done in view of background rejection.

plot the  $\Delta R$  separation between the two light Higgs states. For a light Higgs boson mass of  $m_h = 40$  GeV, it is clear (since  $\Delta R \approx \pi$ ) that the  $H \rightarrow hh$  decay is dominantly back-to-back (in the laboratory frame). However, for  $m_h = 60$  GeV, there is a double peak structure. This occurs due to a recoil effect from Initial State Radiation (ISR), which only becomes apparent at the mass boundary where  $m_H \simeq 2m_h$ . The inability of the two emerging  $h$  states to fly apart implies some overlapping of the  $b$ -quark momenta. Hence, we expect that the signal, upon enforcing a jet clustering algorithm, will have a rather high  $b$ -jet multiplicity, so long that the two  $b$ -jets stemming from  $h$  decays are resolved, unless detector acceptance and signal selection cuts reduce it, which is quite possible given the light masses considered for the  $h$  state in relations to typical jet  $p_T$  thresholds used in applying  $b$ -tagging. We will investigate this later.

As a final study, in fact, the  $p_T$  of the  $b$ -quarks is plotted. This is done in Fig. 7. From the top histogram we can see that in both mass configurations the  $b$ -quarks have a wide range of  $p_T$ 's and hence one would expect the resulting jets to have a similar spread of  $p_T$ 's. In particular, we also plot the highest and lowest  $p_T$ 's amongst the  $b$ -quarks in a given event (bottom-left and bottom-right frames, respectively). Further to the discussion in Sec. 2.2, one would therefore expect the resulting spread of radiation from each signal  $b$ -quark to vary in solid angle and hence the resulting jets be of differing sizes. This thus motivates the need for a jet reconstruction sequence that behaves sensibly for jets of various cone sizes. Therefore, in the next section, we firstly test how jet clustering with fixed- $R$  input behaves and then introduce the variable- $R$  algorithm.

### 3.2 Hadron Level Analysis

We start this section by investigating the performance of jet reconstruction and  $b$ -tagging, in particular, in order to see how often the entire signal of four  $b$ -jets is selected. Initially, a baseline analysis without cuts is performed, using the anti- $k_T$  jet algorithm [16] with (fixed) jet radius parameters  $R = 0.4$  and  $0.8$ . (The results for the CA scheme are very similar, so we refrain from presenting them here.) The corresponding multiplicity of  $b$ -tagged jets is plotted in the top left frame of Fig. 8, where no  $p_T$  cut has been imposed on the  $b$ -jets or to its constituents prior to clustering, thereby exemplifying a ‘perfect’ detector. We find that the majority of the events include four  $b$ -tagged jets. However, notice that, if we follow typical jet selection cuts used in experimental analyses of  $4b$  final states (see our Fig. 5), even with our MC based  $b$ -tagger in action, it is not always possible to reconstruct all the four expected  $b$ -jets (see top-right frame of Fig. 8), as we notice a significant shift towards smaller  $b$ -jet multiplicities in this case ( $R = 0.8$ ), the more so the lighter the  $h$  mass. The pattern is rather similar for  $R = 0.4$  (bottom frames of Fig. 8), albeit less so the heavier the  $h$  mass. Altogether

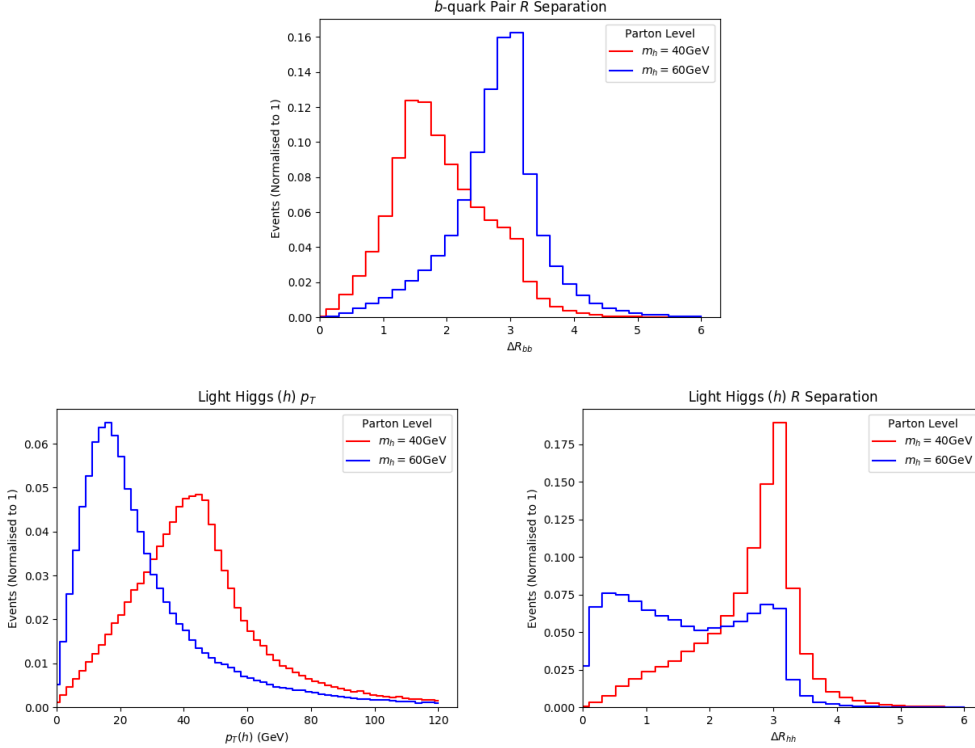


Figure 6: Upper panel: the  $\Delta R$  distribution between the two  $b$ -partons originating from the same  $h$ . Lower panels: (Left) the  $p_T$  distribution of the light Higgs boson  $h$  originating from  $H$  decay; (Right) the  $\Delta R$  distribution between the two  $h$  states originating from the  $H$  decay. The following two mass choices have been considered:  $m_h = 40$  and  $60$  GeV. No (parton level) cuts have been enforced here.

the shift is substantial in both  $R$  cases, to the extent that, in a scenario where the LHC deploys a search with the cuts listed in Fig. 5, the majority of signal events is lost and this is specifically due to the severe  $p_T$  cuts, as can be seen from the (cumulative)  $p_T$  distribution of all  $b$ -jets before cuts, Fig. 9. In fact, from here, it is clear that, no matter the final  $b$ -jet multiplicity, a  $p_T > 30$  GeV cut on all reconstructed jets is very damaging, thereby hinting that somewhat looser cuts on the hadronic system may be desirable (as mentioned in the previous section)<sup>7</sup>. Results for the CA jet algorithm (whatever the  $R$

<sup>7</sup>In fact, we should further notice that the left frames of Fig. 8, i.e., in absence of any cuts, also serve the purpose of quantifying the efficiency of our  $b$ -tagging performance.

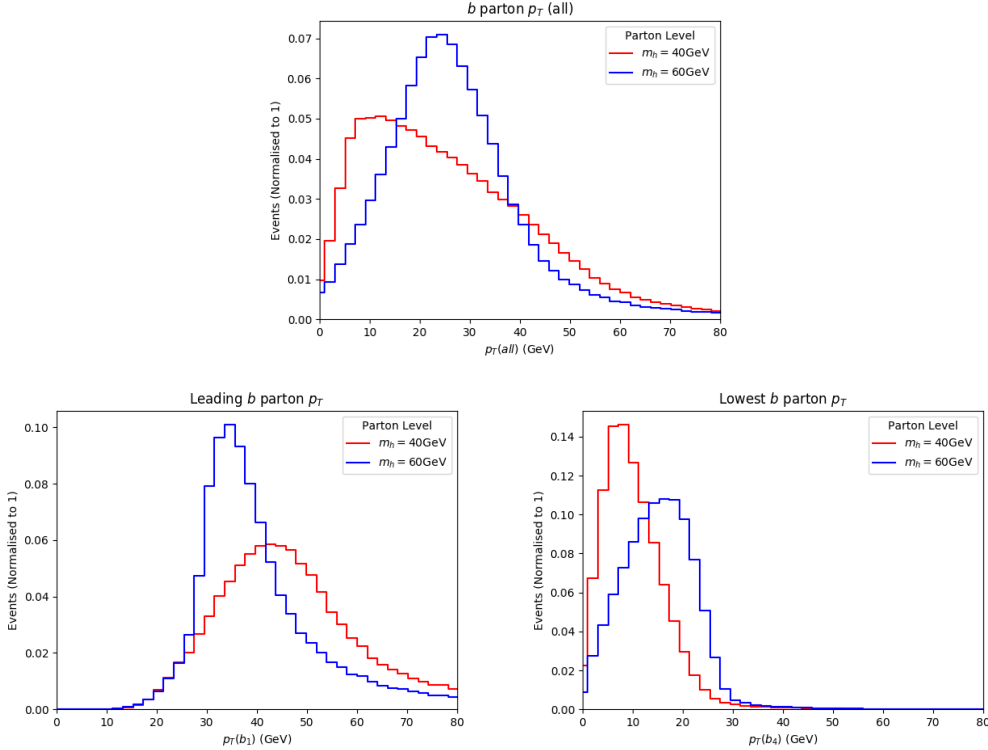


Figure 7: Upper panel: the  $p_T$  distribution for all  $b$ -quarks. Lower panels: (Left) highest  $p_T$  amongst the  $b$ -quarks; (Right) lowest  $p_T$  amongst the  $b$ -quarks. No (parton level) cuts have been enforced here.

value) are not significantly different for any of the observables discussed.

Before addressing the issue of an alternative selection of the hadronic system, we want to discuss some kinematic features of the surviving events. Specifically, the selection that we implement to construct two- and four-jet mass distributions (described below) requires that we select at least three  $b$ -jets. The poor statistics due to these strict cuts does not allow for this, as visible in Fig. 8. Thus, as a test of our ability to reconstruct  $m_h$  and  $m_H$  from two- and four-jet systems, we present distributions for samples before cuts are applied, see Fig. 10. In order to seek out a  $m_h$  resonance in the mass of  $b$ -jet pairs, we select events with three or four  $b$ -jets. For those with three, we compute  $m_{bb}$  for all possible pairs and select the pair minimising  $|m_{bb} - m_h|$ . In the case where all four  $b$ -jets are reconstructed, the same selection is made, but the left-over  $b\bar{b}$  pair is

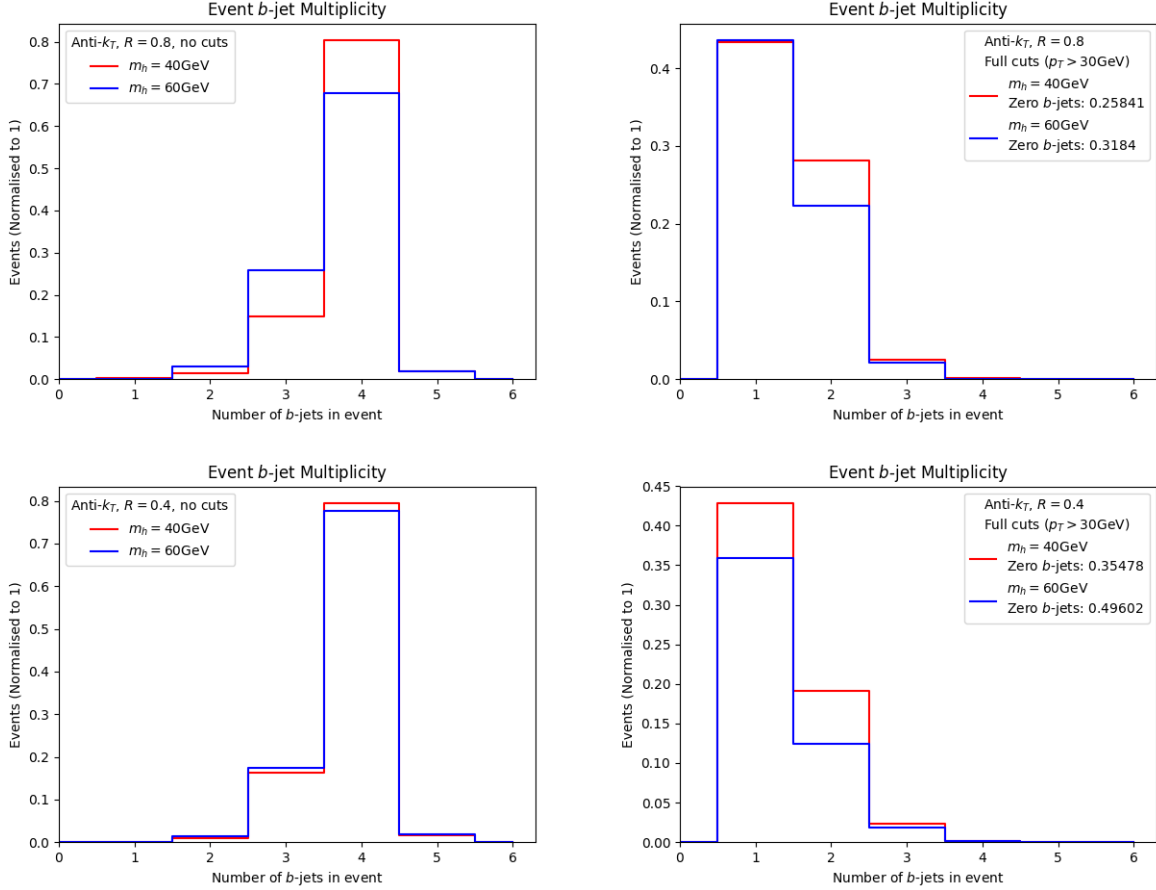


Figure 8: The distributions of  $b$ -jet multiplicities when no cuts are imposed on the jets (left panels) and with the full cutflow described in Fig 5 (right panels). Top(Bottom) panels are for  $R = 0.8(0.4)$ . Here, we have used the anti- $k_T$  jet clustering algorithm. Note that events containing zero  $b$ -jets are not plotted but included in the legend, in the case of no cuts being applied all events contain at least one  $b$ -jet.

also included so as to account for the presence of the second light Higgs state. (Herein, tails are due to inefficiency in this pairing technique and also to fixed cone effects in jets for which  $\Delta R$  is smaller than  $R$ .) Notice the two-jet mass distributions develop a shift of the peaks (from both  $m_h = 40$  and  $60$  GeV), by a few GeV, and that the same effect is present on the four-jet ones (and is even more substantial), amounting to tens of GeV shifts from  $m_H = 125$  GeV. The effect is more marked for smaller (lower frames

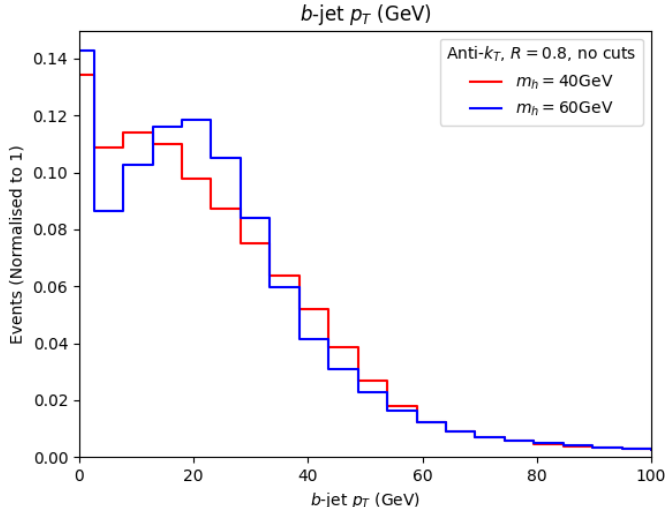


Figure 9: Transverse momentum distribution of all  $b$ -jets with no cuts imposed on the jets or on the final state hadrons. We have used here  $R = 0.8$ , though the pattern is similar for  $R = 0.4$ . Here, we have used the anti- $k_T$  jet clustering algorithm.

in Fig. 10) than larger (upper frames in Fig. 10) cone sizes. We are thus motivated to consider an alternative to a reconstruction using a fixed cone size. Again, results for the CA jet algorithm are not significantly different for any of the observables presented here using the anti- $k_T$  algorithm.

With an improvement of the  $b$ -jet multiplicity in mind, we adopt the lesser cuts described at the end of the previous section: i.e., the leading  $b$ -jet has  $p_T > 20$  GeV while the remaining ones are required to have  $p_T > 15$  GeV [20]. With this revised selection cuts (henceforth, ‘reduced cuts’), the  $b$ -jet multiplicity distribution changes significantly, see Fig. 11. That is, we notice distributions which consistently (i.e., for both  $R$  values adopted) display a better efficiency of the new  $p_T$  cuts in selecting a higher number of  $b$ -jets (compare to the right frames in Fig. 8). In particular, the presence of more events containing all four  $b$ -jets from the signal allows one also to better reconstruct the Higgs masses in multi-jet mass distributions, see Fig. 12.

Before moving on to a signal-to-background analysis in presence of reduced  $p_T$  cuts on the  $b$ -jets, however, there is a further way of improving the proportion of events containing larger  $b$ -jet multiplicities. Referring back to Fig. 8, where, even without cuts, a significant number of  $b$ -jets is already lost in the process of jet reconstruction and tagging, and further noticing, from Fig. 6, that the cone size plays a crucial role

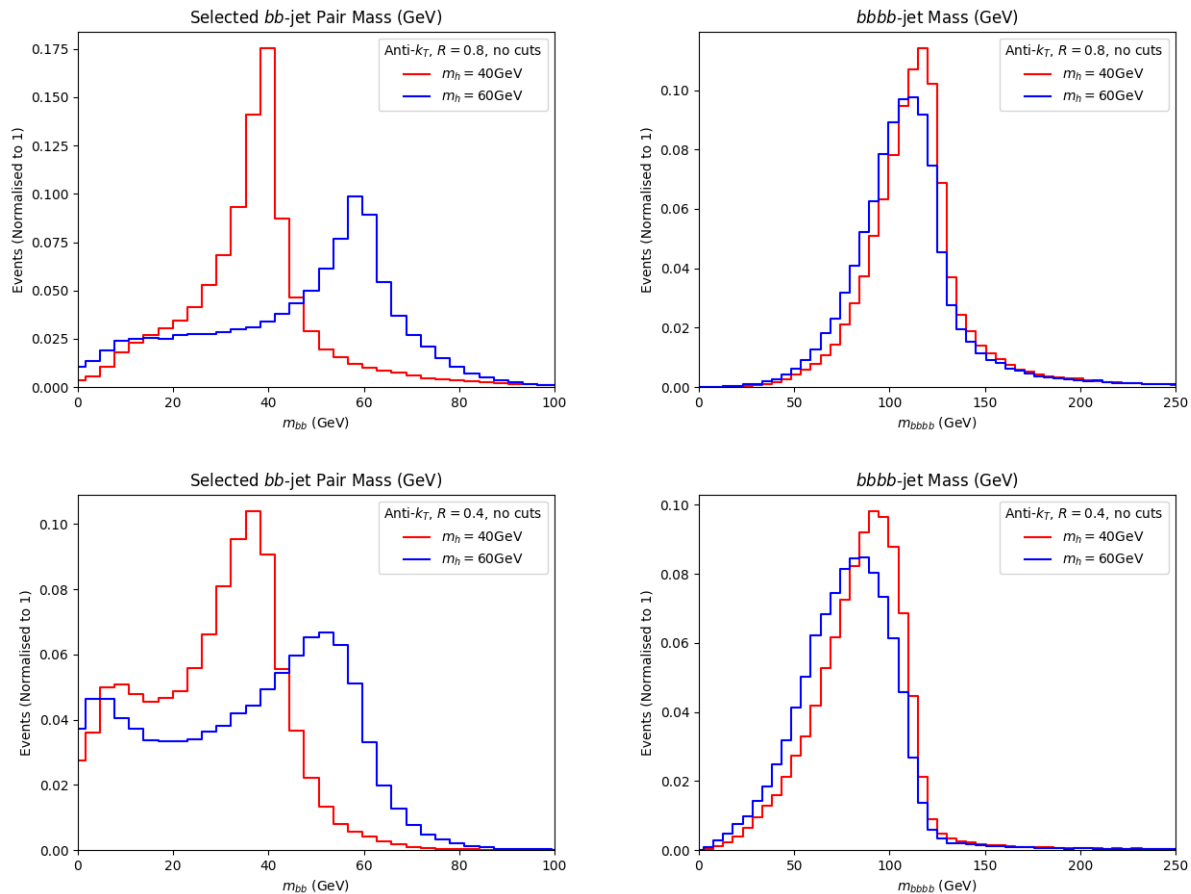


Figure 10: The distributions in invariant mass of two (left panels) and four (right panels)  $b$ -tagged jets. No cuts have been implemented here. Top(Bottom) panels are for  $R = 0.8(0.4)$ . Here, we have used the anti- $k_T$  jet clustering algorithm.

in this respect, it is not surprising that using a ‘variable- $R$ ’ approach to jet clustering (and hence tagging), like the one of Ref. [10], recovers a better multiplicity behaviour from the  $b$ -jet sample before cuts are applied. In this approach, the clustering process is modified, as explained in a previous section, so that one can more efficiently avoid events with very wide jets at low  $p_T$ . The parameter  $\rho$  can be optimised to obtain maximum desired sensitivity. Furthermore, other parameters such as  $R_{\min/\max}$ , which are cut offs for the minimum and maximum allowed  $R_{\text{eff}}$  (that is, if a jet has  $R_{\text{eff}} > R_{\max}$ , it is overwritten and set to  $R_{\text{eff}} = R_{\max}$ , and equivalently for  $R_{\min}$ ). In order to select the

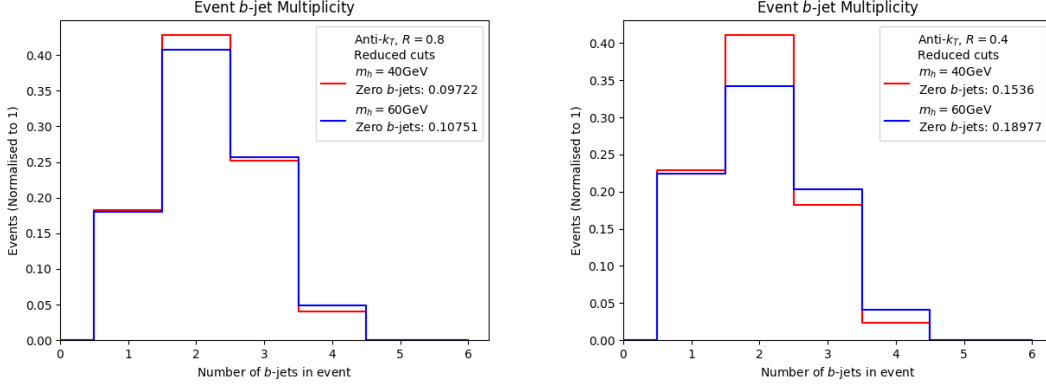


Figure 11: The distributions of  $b$ -jet multiplicities when the cuts in  $p_T$  discussed at the end of the previous section have been implemented here. Left(Right) panel is for  $R = 0.8(0.4)$ . The anti- $k_T$  jet clustering algorithm has been used throughout. Note that events containing zero  $b$ -jets are not plotted but included in the legend.

optimal choice of  $\rho$ , a scan over various values is performed, the results of which are in Fig. 13. To measure each  $\rho$  choice, events are reconstructed and tagged using the standard procedure, with the reduced outflow described in Fig. 5. The  $b$ -jets are then put into pairs based on those best reconstructing the relevant Higgs mass and events are then put through the selection process described later in Fig. 18, after which the number of events passing the selection (normalised to one) is plotted.

From the results in Fig. 13, we chose a value of  $\rho = 20$  GeV for our analysis using variable- $R$  clustering. We select a single value of  $\rho$  for both samples in order to avoid biasing the jet reconstruction to the signal we are searching for, it is however informed by the  $p_T$  scale of the jets. In essence, this variable- $R$  technique helps to construct jets with a cone shape reflecting their true size as measured in the resonance rest frame. Here, we use a variable- $R$  plugin available in the `fastjet-contrib` project (<https://fastjet.hepforge.org/contrib/>). In the left panel of Fig. 14, we show the  $b$ -jet multiplicity using the variable- $R$  algorithm when no cuts are imposed on the  $b$ -tagged jets. Now the proportion of events with all four  $b$ -jets intact is close to unity, which is better than the fixed- $R$  case in Fig. 8. Then, in the right panel of Fig. 14, by applying the reduced cuts on the  $p_T$  of  $b$ -jets, we find a significant improvement in  $b$ -jet multiplicity compared to the fixed- $R$  approaches in Fig. 11. Clearly a greater proportion of jet events with larger  $b$ -jet multiplicities is found in the end for a realistic detector analysis in the case of the variable- $R$  approach, in comparison to the fixed- $R$  one.

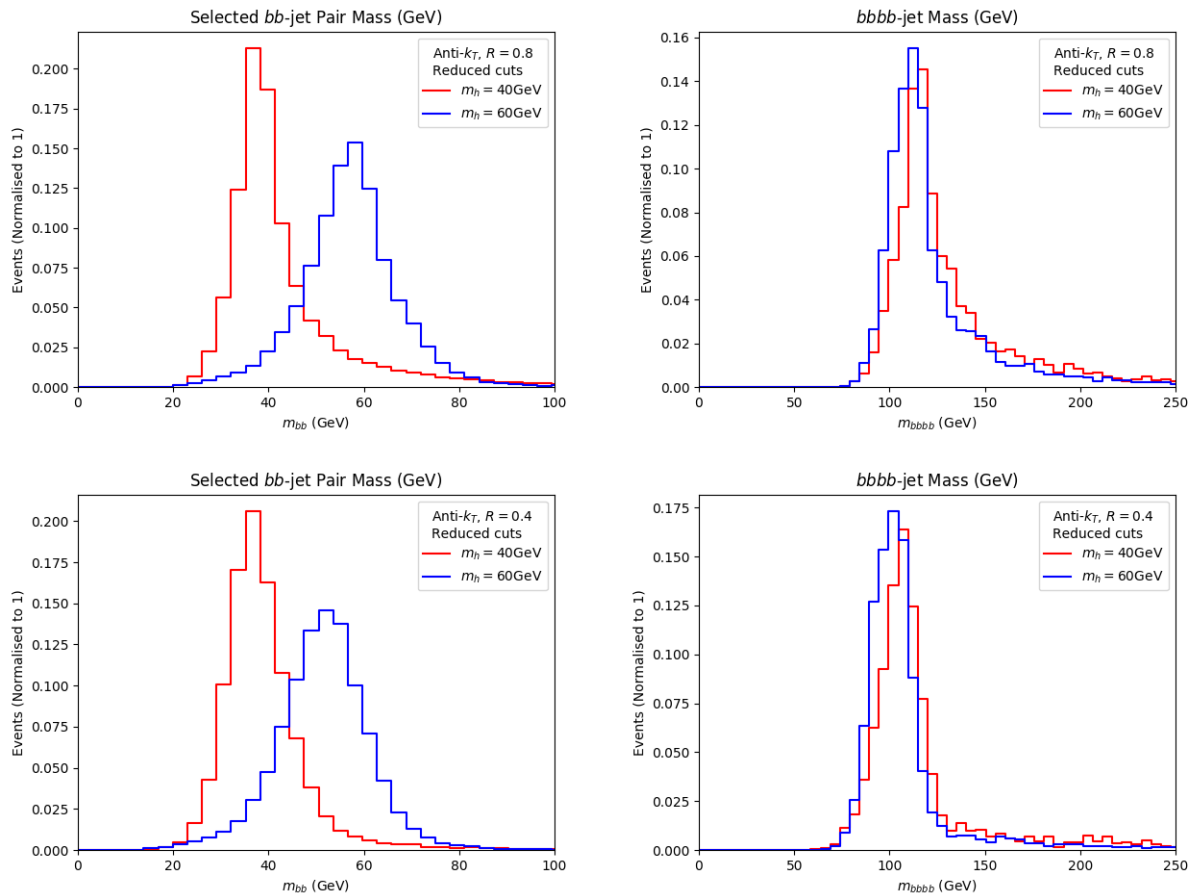


Figure 12: The distributions in invariant mass of two (left panels) and four (right panels)  $b$ -tagged jets, in presence of the reduced  $p_T$  cuts on the  $b$ -jets. Top(Bottom) panels are for  $R = 0.8(0.4)$ . Here, we have used the anti- $k_T$  jet clustering algorithm.

From using the variable- $R$  approach, one can extract which cone sizes have been selected in the clustering procedure. Interestingly, one notices from Fig. 15 that the different  $h$  masses are clustered into  $b$ -jets of different cone sizes. Therefore, as intimated, any experimental search strategy for our signal process using a fixed- $R$  (whether anti- $k_T$ , CA or indeed others) will not be suited to cover the entire range of possible  $m_h$  values. Furthermore, it is also evident that the sample contains  $b$ -jets over a relatively large range of cone sizes. In particular, one can check the  $R_{\text{eff}}$  distribution of  $p_T$  ordered  $b$ -jets. In Fig. 16, we show, in particular, the distributions of  $R_{\text{eff}}$  for the highest and

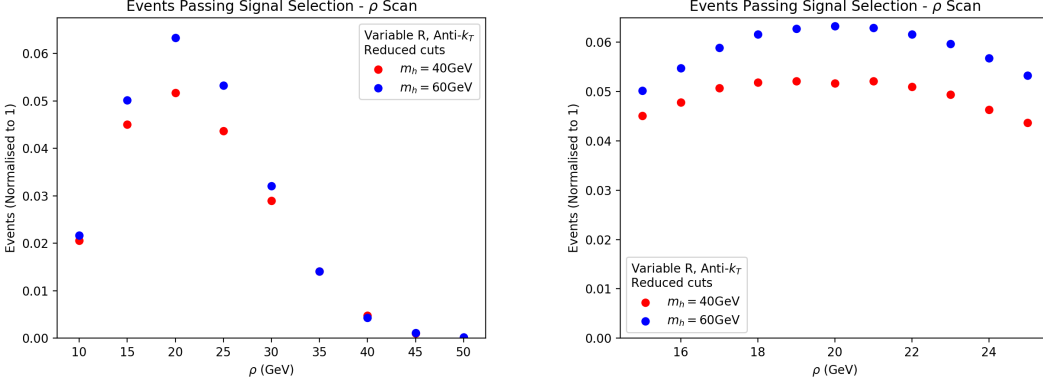


Figure 13: Scan over the  $\rho$  ranges  $[10, 50]$  GeV (left) and  $[15, 25]$  GeV (right) in order to find the the highest number of signal events. Hereafter,  $\rho = 20$  GeV is chosen for both masses.

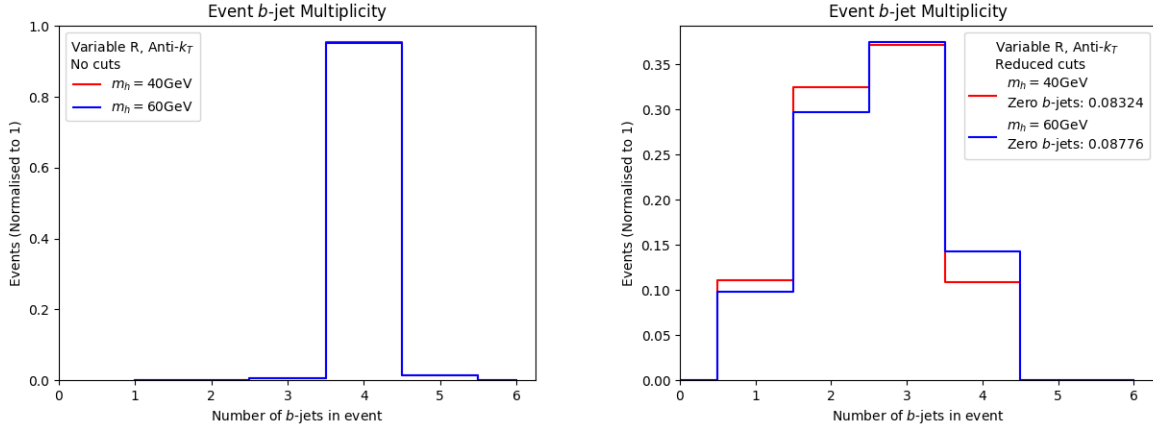


Figure 14: The distributions of  $b$ -jet multiplicities using the variable- $R$  jet clustering algorithm. Left(Right) panel is with no cuts(reduced  $p_T$  cuts) on the  $b$ -jets. Note that events containing zero  $b$ -jets are not plotted but included in the legend, showing that, in the case of no cuts being applied, all events contain at least one  $b$ -jet.

lowest  $p_T$   $b$ -jet, from which it is evident that kinematically unbalanced events (which are far more frequent over the phase space than balanced ones) will be largely depleted, whichever the actual fixed cone size is adopted.

The key issue addressed by the variable- $R$  approach thus becomes apparent. In any

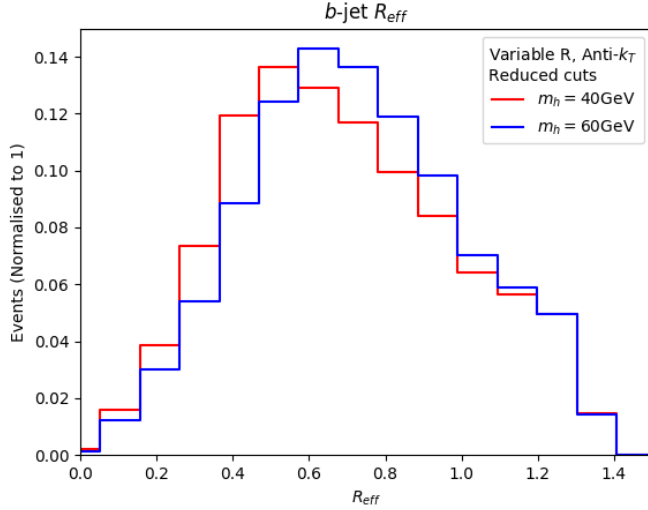


Figure 15: The distributions of  $R_{\text{eff}}$  for all  $b$ -jets computed using the variable- $R$  jet clustering algorithm, upon enforcing the reduced  $p_T$  cuts on the  $b$ -jets.

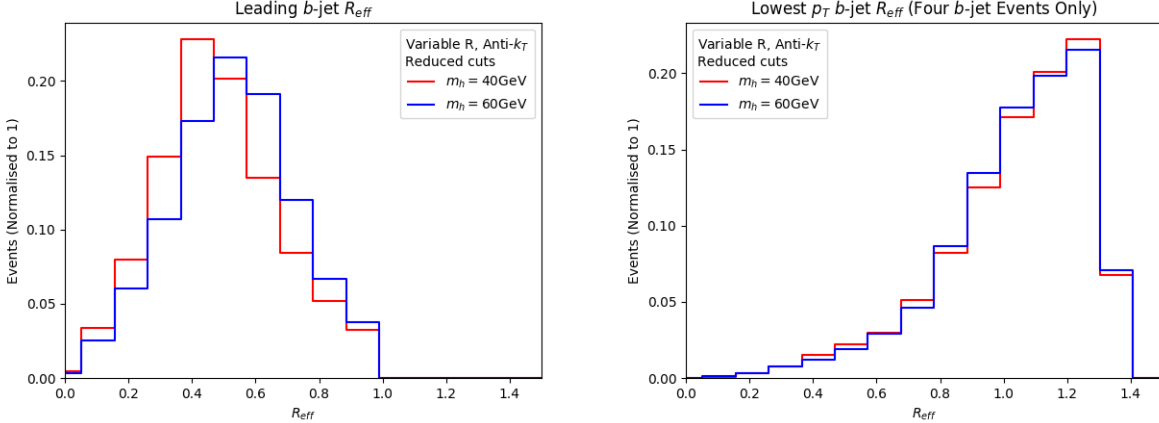


Figure 16: The distributions of  $R_{\text{eff}}$  for the highest (left) and lowest (right)  $p_T$   $b$ -jets computed using the variable- $R$  jet clustering algorithm, upon enforcing the reduced  $p_T$  cuts on the  $b$ -jets.

given event there is a large spread in the cone sizes of the  $b$ -jets coming from our signal process. Using a single fixed- $R$  value will either poorly reconstruct  $m_h$  in di-jet invariant masses as it is too low to capture the entire jet or is too large to distinguish and tag all

four  $b$ -jets, so that this will also adversely impact the  $m_H$  reconstruction. Conversely, using the variable- $R$  approach, it is possible to extract the  $m_H$  and  $m_h$  resonance peaks more efficiently. We construct all possible di-jet invariant masses for events with at least two  $b$ -tagged jets and select the one closest to the true light Higgs mass. From the left plot of Fig. 17, one can observe a very neatly reconstructed peak at the light Higgs boson mass. Furthermore, the four  $b$ -jet invariant mass is also efficiently reproduced around the true heavy Higgs boson mass, right plot of Fig. 17. Now, contrast these mass spectra with those in Fig. 12, in relation to both peak sharpness and location, to conclude that we have been able to significantly improve the potential of extracting our signal and characterise it in terms of the underlying kinematic features. We now ought to implement the same procedure in the case of the relevant backgrounds, which we will do next.

### 3.3 Signal-to-Background Analysis

As a final exercise, we perform a calculation of the signal-to-background rates, so as to compare the various jet reconstruction procedures mentioned in this paper also in connection with their performance in dealing with events not coming from our BSM process. In order to do so, we perform the selection procedure described in Fig. 18, which bolts on the discussed reduced  $p_T$  cuts. We use the anti- $k_T$  measure throughout but conclusions would not change in case of the CA one.

Tab. 2 contains the cross sections in pb for signal and the various background processes upon applying the aforementioned cuts and mass selections. It is clear from the data obtained that the QCD-induced  $pp \rightarrow b\bar{b}b\bar{b}$  process is the dominant background channel<sup>8</sup>, followed by  $pp \rightarrow Zb\bar{b}$  and  $pp \rightarrow t\bar{t}$ . Our next step is then to calculate the event rates in order to get the significances for two values of (integrated) luminosity, e.g.,  $\mathcal{L} = 140$  and  $300 \text{ fb}^{-1}$ , corresponding to full Run 2 and 3 data samples, respectively. The event rate ( $N$ ) for the various processes is given by:

$$N = \sigma \times \mathcal{L}. \quad (5)$$

Tabs. 3–4 contain  $N$  values for the two given luminosities, 140 and  $300 \text{ fb}^{-1}$ , respectively. After the event rates have been calculated, we simply evaluate the significance,  $\Sigma$ , which is given by (as a function of signal  $S$  and respective background  $B$  rates)

$$\Sigma = \frac{N(S)}{\sqrt{N(B_{b\bar{b}b\bar{b}}) + N(B_{Zb\bar{b}}) + N(B_{t\bar{t}})}}. \quad (6)$$

---

<sup>8</sup>In fact, we have computed the full four-jet sample produced by QCD, i.e., including all four-body partonic final states, yet, in presence of the described kinematical selections and  $b$ -tagging performances, the number of non- $b\bar{b}b\bar{b}$  events surviving is negligible.

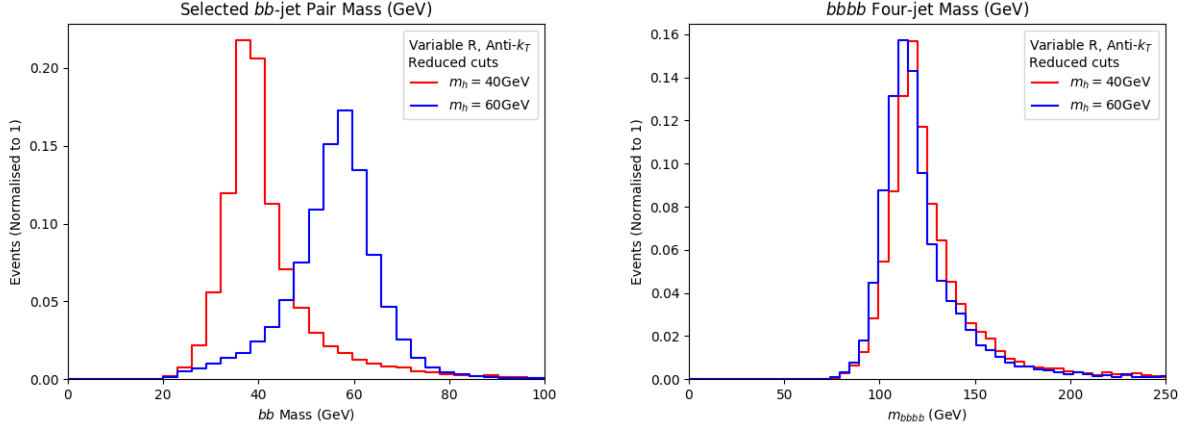


Figure 17: The distributions in invariant mass of two (left) and four (right)  $b$ -tagged jets, in presence of the reduced  $p_T$  cuts on the  $b$ -jets. Here, we have used the variable- $R$  jet clustering algorithm.

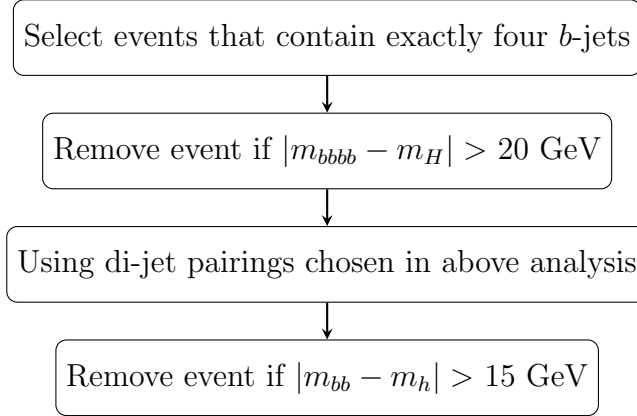


Figure 18: Event selection used to compute the signal-to-background rates.

It is then clear from Tabs. 5–6 that the variable- $R$  approach works better than the fixed- $R$  one also in providing the best significances, no matter the choices of  $R$  for the latter. The improvement in the final significances is indeed very significant. This should not be surprising, given the ability of the former in outperforming the latter from the point of view of kinematics. For completeness, we finally present in Figs. 19–20 the  $m_{bb}$  and  $m_{bbbb}$  spectra, as previously described, for the signals and three most relevant backgrounds (i.e., the aforementioned  $b\bar{b}b\bar{b}$ ,  $Zb\bar{b}$  and  $t\bar{t}$ ). Again, while the signal-to-

background analysis has been performed for the anti- $k_T$  algorithm, the same conclusions are reached for the CA case.

Process	Var-R, $\rho = 20$ GeV		$R = 0.4$		$R = 0.8$	
	40 GeV	60 GeV	40 GeV	60 GeV	40 GeV	60 GeV
$pp \rightarrow H \rightarrow hh \rightarrow bbbb$	$5.729 \times 10^{-3}$	$1.306 \times 10^{-1}$	$8.483 \times 10^{-4}$	$1.658 \times 10^{-2}$	$1.813 \times 10^{-3}$	$4.193 \times 10^{-2}$
$pp \rightarrow t\bar{t}$	$1.226 \times 10^{-2}$	$1.635 \times 10^{-2}$	$4.088 \times 10^{-3}$	$1.022 \times 10^{-2}$	$2.044 \times 10^{-3}$	$2.044 \times 10^{-3}$
$pp \rightarrow bbbb$	$3.559 \times 10^1$	$5.335 \times 10^1$	$2.667 \times 10^1$	8.891	$1.779 \times 10^1$	$2.491 \times 10^1$
$pp \rightarrow Zbb$	$1.797 \times 10^{-1}$	$2.471 \times 10^{-1}$	$2.246 \times 10^{-2}$	$4.643 \times 10^{-2}$	$7.489 \times 10^{-2}$	$7.339 \times 10^{-2}$

Table 2: Cross sections (in pb) of signal and background processes upon enforcing the reduced cuts plus the mass selection criteria  $|m_{bbbb} - m_H| < 20$  GeV and  $|m_{bb} - m_h| < 15$  GeV for the various jet reconstruction procedures.

Process	Var-R, $\rho = 20$ GeV		$R = 0.4$		$R = 0.8$	
	40 GeV	60 GeV	40 GeV	60 GeV	40 GeV	60 GeV
$pp \rightarrow H \rightarrow hh \rightarrow bbbb$	802.186	18295.55	118.762	2322.054	253.862	5870.676
$pp \rightarrow t\bar{t}$	1717.052	2289.403	572.350	1430.877	286.175	286.175
$pp \rightarrow bbbb$	4983804	7469163.8	3734581.2	1244860.54	2491902	3488662.8
$pp \rightarrow Zbb$	25164.272	34600.874	3145.534	6500.769	10485.112	10275.409

Table 3: Event rates of signal and backgrounds for  $\mathcal{L} = 140 \text{ fb}^{-1}$  upon enforcing the reduced cuts plus the mass selection criteria  $|m_{bbbb} - m_H| < 20$  GeV and  $|m_{bb} - m_h| < 15$  GeV for the various jet reconstruction procedures.

Process	Var-R, $\rho = 20$ GeV		$R = 0.4$		$R = 0.8$	
	40 GeV	60 GeV	40 GeV	60 GeV	40 GeV	60 GeV
$pp \rightarrow H \rightarrow hh \rightarrow bbbb$	1718.97	39204.75	254.49	4975.83	543.99	12580.02
$pp \rightarrow t\bar{t}$	3679.398	4905.864	1226.466	3066.165	613.233	613.233
$pp \rightarrow bbbb$	10679580	16005351	8002674	2667558.3	5339790	7475706
$pp \rightarrow Zbb$	53923.44	74144.73	6740.43	13930.221	22468.098	22018.734

Table 4: Event rates of signal and backgrounds for  $\mathcal{L} = 300 \text{ fb}^{-1}$  upon enforcing the reduced cuts plus the mass selection criteria  $|m_{bbbb} - m_H| < 20$  GeV and  $|m_{bb} - m_h| < 15$  GeV for the various jet reconstruction procedures.

### 3.4 Discussion

Before concluding, we review here some other studies from the literature utilising a variable- $R$  reconstruction procedure.

	Var-R, $\rho = 20$ GeV	$R = 0.4$	$R = 0.8$
40 GeV	0.358	0.061	0.160
60 GeV	6.677	2.074	3.138

Table 5: Final  $\Sigma$  values calculated for signal and backgrounds for  $\mathcal{L} = 140 \text{ fb}^{-1}$  upon enforcing the reduced cuts plus the mass selection criteria  $|m_{bbbb} - m_H| < 20 \text{ GeV}$  and  $|m_{bb} - m_h| < 15 \text{ GeV}$  for the various jet reconstruction procedures.

	Var-R, $\rho = 20$ GeV	$R = 0.4$	$R = 0.8$
40 GeV	0.524	0.089	0.234
60 GeV	9.775	3.036	4.594

Table 6: Final  $\Sigma$  values calculated for signal and backgrounds for  $\mathcal{L} = 300 \text{ fb}^{-1}$  upon enforcing the reduced cuts plus the mass selection criteria  $|m_{bbbb} - m_H| < 20 \text{ GeV}$  and  $|m_{bb} - m_h| < 15 \text{ GeV}$  for the various jet reconstruction procedures.

In Fig. 16 we note that, while the leading  $b$ -jet has an  $R_{\text{eff}}$  roughly in line with expected values ( $R_{\text{eff}} \simeq 0.5$ ), the lowest  $p_T$   $b$ -jets have large cone sizes ( $R_{\text{eff}} > 1.0$ ), risking potential contamination from additional radiation. This effect is discussed in [31]. We do not implement any vetoes to remedy this effect, yet, despite this, our results still suggest that the variable- $R$  approach displays an improvement over traditional methods.

There have been other studies utilising variable- $R$  methods for physics searches. For example, in highly boosted object tagging of  $hh \rightarrow b\bar{b}b\bar{b}$  decays in [32]. Furthermore, in [31] mentioned above, a variable- $R$  algorithm is deployed in the context of heavy particle decays. In both examples, an improvement over current fixed- $R$  methods is present when using variable- $R$ , which is in line with our findings.

As a final word on using variable- $R$  jet reconstruction in experiments, we discuss its use in relation to  $b$ -tagging performance. In particular, the studies [33, 34] explore the possibility of Higgs to  $b$ -jet tagging at ATLAS using variable- $R$  techniques. Specifically, these studies deal with boosted topologies, focusing on fat  $b$ -jet substructure, so the validity of applying these techniques in a non-boosted regime is to be determined.

## 4 Conclusions

In this paper, we have assessed the potential scope of the LHC experiments in accessing BSM Higgs signals induced by cascade decays of the 125 GeV SM-like Higgs state discovered in July 2012, through the following prototypical production and decay channel:

$gg \rightarrow H \rightarrow hh$ , where  $H$  is the SM-like Higgs state and  $h$  is a lighter BSM Higgs state, with mass less than  $m_H/2$ , so as to induce resonant production and decay, thereby enhancing the overall rate. Any such a  $h$  boson, largely independently of the BSM construct hosting it, would decay to  $b\bar{b}$  pairs, eventually leading to a four  $b$ -jet signature. The latter is extremely difficult to establish at the LHC, owing to the substantial hadronic background. Therefore,  $b$ -tagging techniques are to be exploited in order to make such a signal visible. However, this poses the problem that the latter are most efficient at large transverse momentum of the  $b$ -jets, say at least 20 GeV, which in turn corresponds to a significant loss of signal events if the BSM Higgs mass is in the sub-60 GeV range. Hence, if one intends to maximise sensitivity to this benchmark signature of BSM physics, a thorough reassessment of the current Run 2 approaches is mandated for, and especially so in view of the upcoming Run 3.

The first message we deliver is that, with current  $p_T$  limitations on final state  $b$ -jets, using a fixed- $R$  jet reconstruction and tagging procedure will lead to a poor signal visibility, with a majority of signal  $b$ -jets being lost. We instead presented a reduced cut flow, based on existing  $b\bar{b}\mu^+\mu^-$  analyses, and showed that this indeed provides a window onto  $gg \rightarrow H \rightarrow hh \rightarrow b\bar{b}b\bar{b}$  signals with  $m_H = 125$  GeV and  $m_h < \frac{m_H}{2}$ .

Additionally, and perhaps more remarkably, we also tested a variable- $R$  reconstruction approach on events with this reduced cut flow and showed a significant improvement in signal yield as well as signal-to-background rates. We notice that in final states of this kind, the signal  $b$ -jets have a wide range of  $p_T$  and hence varied spread of constituents. Using a fixed cone of a standard size ( $R = 0.4$ ) well constructs higher  $p_T$  jets in an event but does not capture much of the wider angle radiation from lower  $p_T$  jets. This leads to two issues. Firstly, it will prove difficult to accurately construct  $m_h$  and  $M_H$  in the two- and four-jet invariant masses. Secondly, these jets will more often be lost due to kinematic cuts. A larger cone ( $R = 0.8$ ), conversely, will gather up too much ‘junk’ in the higher  $p_T$  jets, which again will contaminate the signal.

As we have obtained all of the above in presence of a sophisticated MC event simulation, based on exact scattering MEs, state-of-the-art parton shower, hadronisation and  $B$ -hadron decays as well as a realistic detector simulation, we recommend deployment of our envisaged selection strategy in future LHC analyses aiming at extracting the aforementioned decay chain. In fact, while we have quantitatively based our case on the example of the 2HDM-II (wherein  $h$  was the lightest CP-even Higgs state, yet it could equally have been the CP-odd one,  $A$ ), our procedure can identically be used in other BSM constructs featuring light (pseudo)scalar states emerging from decays of the SM-like Higgs state and in turn decaying into  $b\bar{b}$  pairs.

## Acknowledgments

SM is supported also in part through the NExT Institute and the STFC Consolidated Grant No. ST/L000296/1. BF is funded by the DISCnet SEPnet scholarship scheme. The work of AC is funded by the Department of Science and Technology, Government of India, under Grant No. IFA18-PH 224 (INSPIRE Faculty Award). We all thank G.P. Salam for useful advice. We also give thanks to Benjamin Fuks, Eric Conte and others in the MadAnalysis5 team for their assistance with technical queries. BF and SJ acknowledge the use of the IRIDIS High Performance Computing Facility, and associated support services at the University of Southampton, in the completion of this work.

## References

- [1] G. Aad *et al.* [ATLAS Collaboration], Phys. Lett. B **716** (2012) 1 [[arXiv:1207.7214](#) [hep-ex]].
- [2] K. Shaaban and S. Moretti,, “Supersymmetry Beyond Minimality: from Theory to Experiment”, CRC Press (Taylor & Francis), 2017.
- [3] U. Ellwanger, C. Hugonie and A. M. Teixeira, Phys. Rept. **496** (2010) 1 [[arXiv:0910.1785](#) [hep-ph]].
- [4] J. F. Gunion, H. E. Haber, G. L. Kane and S. Dawson, Front. Phys. **80** (2000) 1.
- [5] J. F. Gunion, H. E. Haber, G. L. Kane and S. Dawson, [hep-ph/9302272](#).
- [6] G. C. Branco, P. M. Ferreira, L. Lavoura, M. N. Rebelo, M. Sher and J. P. Silva, Phys. Rept. **516** (2012) 1 [[arXiv:1106.0034](#) [hep-ph]].
- [7] S. Moretti and W. J. Stirling, Phys. Lett. B **347** (1995) 291 Erratum: [Phys. Lett. B **366** (1996) 451] [[hep-ph/9412209](#), [hep-ph/9511351](#)].
- [8] A. Djouadi, J. Kalinowski and P. M. Zerwas, Z. Phys. C **70** (1996) 435 [[hep-ph/9511342](#)].
- [9] L. Scodellaro [ATLAS and CMS Collaborations], [arXiv:1709.01290](#) [hep-ex].
- [10] D. Krohn, J. Thaler and L. T. Wang, JHEP **0906** (2009) 059 [[arXiv:0903.0392](#) [hep-ph]].
- [11] G. F. Sterman and S. Weinberg, Phys. Rev. Lett. **39** (1977) 1436.

- [12] S. Moretti, L. Lonnblad and T. Sjostrand, JHEP **9808** (1998) 001 [[hep-ph/9804296](#)].
- [13] M. Cacciari, G. P. Salam and G. Soyez, Eur. Phys. J. C **72** (2012) 1896 [[arXiv:1111.6097](#) [hep-ph]].
- [14] M. Wobisch and T. Wengler, In \*Hamburg 1998/1999, Monte Carlo generators for HERA physics\* 270-279 [[hep-ph/9907280](#)].
- [15] Y. L. Dokshitzer, G. D. Leder, S. Moretti and B. R. Webber, JHEP **9708** (1997) 001 [[hep-ph/9707323](#)].
- [16] M. Cacciari, G. P. Salam and G. Soyez, JHEP **0804** (2008) 063 [[arXiv:0802.1189](#) [hep-ph]].
- [17] G. P. Salam, Eur. Phys. J. C **67** (2010) 637 [[arXiv:0906.1833](#) [hep-ph]].
- [18] A. M. Sirunyan *et al.* [CMS Collaboration], JINST **13** no. 5 (2018) 05011 [[arXiv:1712.07158](#) [physics.ins-det]].
- [19] A. M. Sirunyan *et al.* [CMS Collaboration], Tech. Rep. CMS-DP-2018-058 (2018).
- [20] A. M. Sirunyan *et al.* [CMS Collaboration], Phys. Lett. B **795** (2019) 398 [[arXiv:1812.06359](#) [hep-ex]].
- [21] D. Eriksson, J. Rathsmann and O. Stål, Comput. Phys. Commun. **181** (2010) 833.
- [22] P. Bechtle, O. Brein, S. Heinemeyer, O. Stål, T. Stefaniak, G. Weiglein and K. E. Williams, Eur. Phys. J. C **74** no. 3 (2014) 2693 [[arXiv:1311.0055](#) [hep-ph]].
- [23] P. Bechtle, S. Heinemeyer, O. Stål, T. Stefaniak and G. Weiglein, Eur. Phys. J. C **74** no.2 (2014) 2711 [[arXiv:1305.1933](#) [hep-ph]].
- [24] F. Mahmoudi, Comput. Phys. Commun. **180** (2009) 1718.
- [25] R. D. Ball *et al.* [NNPDF Collaboration], JHEP **1504** (2015) 040 [[arXiv:1410.8849](#) [hep-ph]].
- [26] J. Alwall *et al.*, JHEP **1407** (2014) 079 [[arXiv:1405.0301](#) [hep-ph]].
- [27] T. Sjostrand, S. Mrenna and P. Z. Skands, Comput. Phys. Commun. **178** (2008) 852 [[arXiv:0710.3820](#) [hep-ph]].

- [28] E. Conte, B. Fuks and G. Serret, *Comput. Phys. Commun.* **184** (2013) 222 [[arXiv:1206.1599](#) [hep-ph]].
- [29] E. Conte and B. Fuks, *Int. J. Mod. Phys. A* **33** no. 28 (2018) 1830027 [[arXiv:1808.00480](#) [hep-ph]].
- [30] A. M. Sirunyan *et al.* [CMS Collaboration], *Phys. Lett. B* **803** (2020) 135285 [[arXiv:1909.05306](#) [hep-ex]].
- [31] T. Lapsien, R. Kogler and J. Haller, *Eur. Phys. J. C* **76** no. 11 (2016) 600 [[arXiv:1606.04961](#) [hep-ph]].
- [32] The ATLAS collaboration [ATLAS Collaboration], ATL-PHYS-PUB-2016-013.
- [33] The ATLAS collaboration [ATLAS Collaboration], ATL-PHYS-PUB-2017-010.
- [34] The ATLAS collaboration [ATLAS Collaboration], ATLAS-CONF-2020-007.

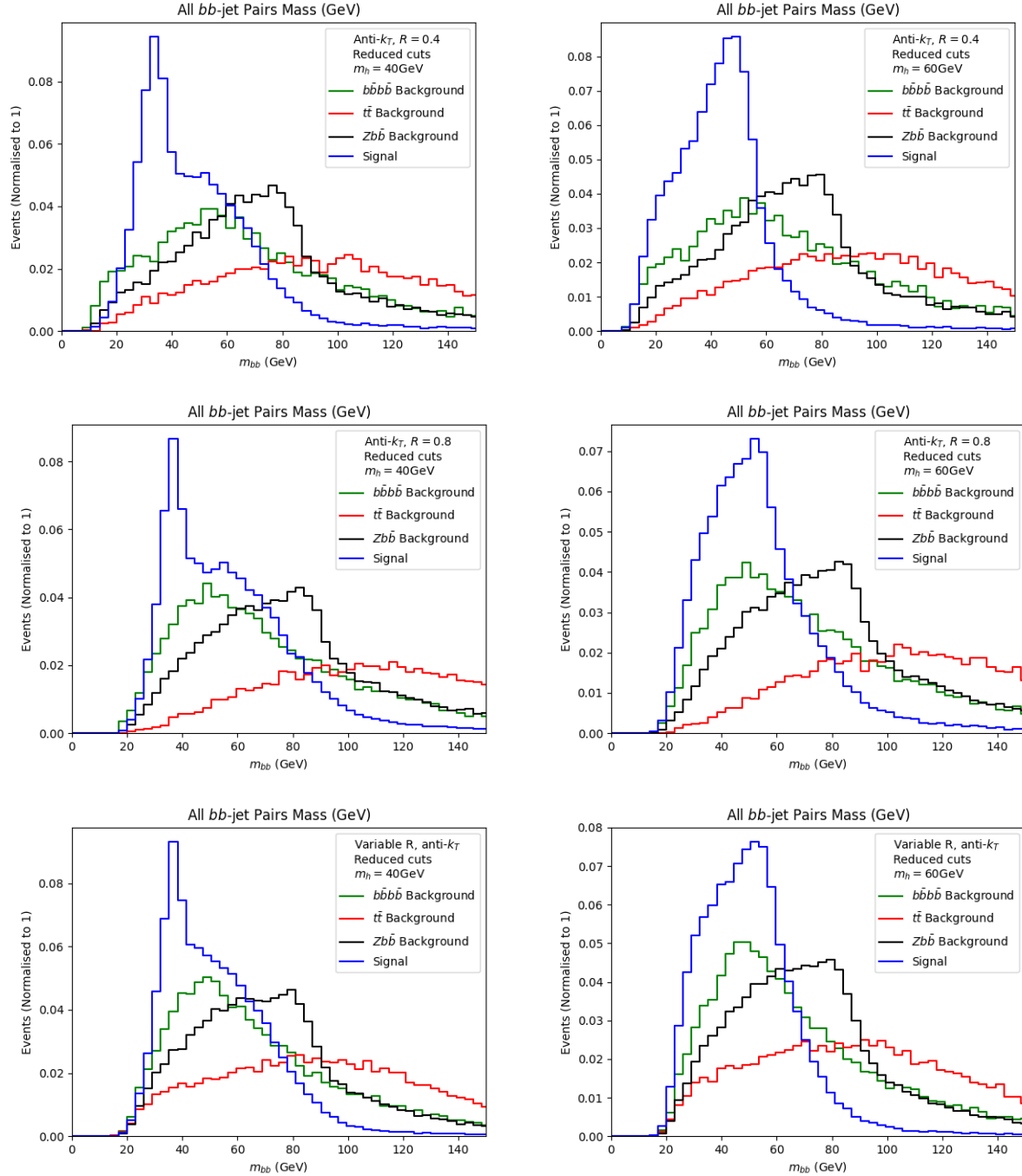


Figure 19: The distributions in invariant mass of two  $b$ -jets for signal and backgrounds after the reduced  $p_T$  cuts plus the discussed mass selections for fixed- $R$  ( $R = 0.4$  at the top and  $0.8$  in the middle) and variable- $R$  ( $\rho = 20$  GeV at the bottom) jet clustering.

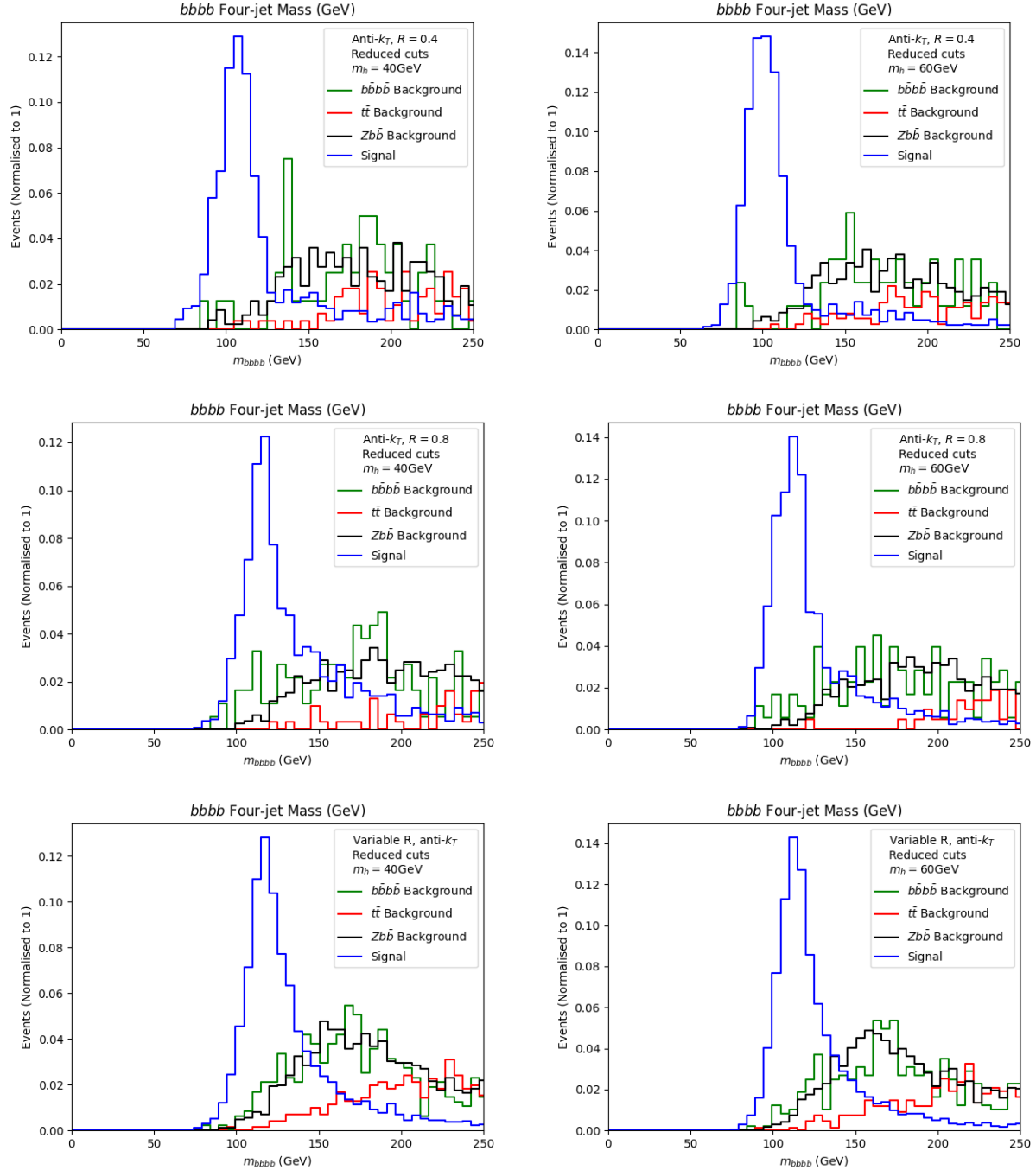


Figure 20: The distributions in invariant mass of four  $b$ -jets for signal and backgrounds after the reduced  $p_T$  cuts plus the discussed mass selections for fixed- $R$  ( $R = 0.4$  at the top and 0.8 in the middle) and variable- $R$  ( $\rho = 20$  GeV at the bottom) jet clustering.